

## Energetic Proton Back-Precipitation onto the Solar Atmosphere in Relation to Long-Duration Gamma-Ray Flares

A. HUTCHINSON,<sup>1</sup> S. DALLA,<sup>1</sup> T. LAITINEN,<sup>1</sup> G. A. DE NOLFO,<sup>2</sup> A. BRUNO,<sup>2,3</sup> AND J. M. RYAN<sup>4</sup>

<sup>1</sup>*University of Central Lancashire, Preston, PR1 2HE, UK*

<sup>2</sup>*NASA Goddard Space Flight Center, Greenbelt, MD, USA*

<sup>3</sup>*Department of Physics, Catholic University of America, Washington DC, USA*

<sup>4</sup>*University of New Hampshire, Durham, NH, USA*

Submitted to ApJ

### ABSTRACT

Gamma-ray emission during Long-Duration Gamma-Ray Flare (LDGRF) events is thought to be caused mainly by  $> 300$  MeV protons interacting with the ambient plasma at or near the photosphere. Prolonged durations of the gamma-ray emission have prompted the suggestion that the source of the energetic protons is acceleration at a CME-driven shock, followed by particle back-precipitation onto the solar atmosphere over extended times. We study the latter phenomenon by means of test particle simulations, which allow us to investigate the effect of magnetic mirroring, which impedes back-precipitation by reflecting particles as they travel sunwards, and of scattering associated with turbulence in the magnetic field. The precipitation fraction,  $P$ , the proportion of protons that successfully precipitate for injection at a fixed height,  $r_i$ , is studied as a function of  $r_i$  and scattering mean free path,  $\lambda$ . We characterise how  $P$  decreases with increasing radial distance, obtaining a dependence of  $r_i^{-1.78}$  for  $\lambda = 0.1$  AU, and we find that the presence of moderate scattering helps back-precipitation compared to the scatter-free case. We determine the total precipitation fraction for eight LDGRF events, finding that it is very small, between 0.23 and 1.99%. Time-extended acceleration and large total precipitation fractions, as seen in the observations, cannot be reconciled for a moving shock source according to our simulations. These results challenge the CME-shock source scenario as the main mechanism for  $\gamma$ -ray production in LDGRFs.

### 1. INTRODUCTION

The production of solar  $\gamma$ -rays over extended durations, including times when flare emission in other wavelengths is no longer present, has been observed for decades in association with large energy release events at the Sun (Ryan (2000) and references therein). In recent years, however, new data at photon energies  $> 100$  MeV from the *Fermi* Large Area Telescope (LAT) have showed that these Long-Duration Gamma-Ray Flares (LDGRFs) are not as rare as previously thought and have reignited debate over their origin (Omodei et al. (2018); Pesce-Rollins et al. (2015); Ackermann et al. (2017); Share et al. (2018); Klein et al. (2018); de Nolfo et al. (2019); Kahler et al. (2018) and references therein). In these events,  $\gamma$ -rays are thought to be generated when

$>300$  MeV protons and  $>200$  MeV/nuc  $\alpha$ -particles collide with the ambient plasma produce pions that subsequently decay near the solar surface ( $1 R_{\odot}$ ) (eg Share et al. (2018) and references therein).

LDGRFs imply that highly energetic protons and  $\alpha$ -particles strike the photosphere over extended time periods, of the order of hours and up to about 20 hours. A number of possible theories for the phenomenon have been put forward. The two main scenarios at the centre of the current debate are: a) trapping of flare accelerated ions within large coronal loops, with the possibility of time-extended acceleration within them (Mandzhavidze & Ramaty 1992; Ryan & Lee 1991) and b) time-extended acceleration at a propagating Coronal Mass Ejection (CME) driven shock followed by back-precipitation onto the solar atmosphere (Cliver et al. 1993). The latter scenario has been referred to as Late-Phase Gamma-Ray Emission (LPGRE) (Share et al.

2018) and Sustained Gamma-Ray Emission (SGRE) (Kahler et al. 2018).

Share et al. (2018) and Winter et al. (2018) analysed the association of LDGRFs with soft-X-ray flares, CMEs and near-Earth Solar Energetic Particle (SEP) events and concluded that their most likely origin is back-precipitation after acceleration at a CME-driven shock. This scenario is also supported by analysis of type II radio burst data (Gopalswamy et al. 2018) and by the energy released from magnetic reconnection in flaring active regions (Kahler et al. 2018). On the other hand, a study of a variety of electromagnetic emissions for a specific event has concluded that reacceleration of particles trapped on closed coronal loops is the most likely explanation for the observed  $\gamma$ -ray signatures (Grechnev et al. 2018). Work by Kong et al. (2019) has shown that acceleration of protons to sufficient energies to produce  $\gamma$ -rays is possible at the flanks of the shock, in close proximity to the solar surface due to interactions with streamers in the corona. This mechanism may favour time-extended  $\gamma$ -ray production via particle trapping in the closed coronal loops associated with streamers.

The back-precipitation scenario has been studied by modelling both the shock acceleration and propagation to the solar surface of the energetic protons. Kocharov et al. (2015) concluded that the mechanism is a viable explanation for LDGRFs but pointed out that only about 1% of the particles accelerated at the shock back-precipitate to the required height. Afanasiev et al. (2018) used a model with strong scattering in the region behind the shock to show that a number of protons sufficient to produce the observed gamma-ray emission (or in some cases considerably larger) propagates to the solar surface. Kouloumvakos et al. (2020) recently presented a study of the 2017 September 10 LDGRF event where they modelled the parameters of the associated CME-driven shock. They conclude that the evolution of the shock and shock orientation can explain the time-history of the  $\gamma$ -ray emission observed by *Fermi* LAT, providing further evidence for the CME-driven shock scenario.

Hudson (2018) and Klein et al. (2018) pointed out that magnetic mirroring is a major obstacle for proton back-propagation from a CME-driven shock to heliocentric distances  $r \sim 1R_{\odot}$ , where  $\gamma$ -ray emission takes place. Because of the solar wind expansion and associated  $1/r^2$  dependence of the magnetic field magnitude, in the absence of scattering, only particles in a very narrow range of pitch-angles (the so-called loss cone) are able to avoid reflection as they move towards the Sun. An open question is how this picture is modified by scattering associated with magnetic field turbulence.

de Nolfo et al. (2019) compared the number of interacting  $\gamma$ -ray-producing protons at the Sun for 14 LDGRF events,  $N_{LDGRF}$ , with the number of protons detected in interplanetary space at 1 AU,  $N_{SEP}$ . The values of  $N_{LDGRF}$  are inferred from *Fermi*/LAT while  $N_{SEP}$  is constrained by *PAMELA* and the twin *STEREO* observations. They found no correlation between  $N_{LDGRF}$  and  $N_{SEP}$  and showed that in several events their ratio is close to 1, implying that back-precipitation of a very large fraction of the energetic particles would be required to explain the events within the CME shock acceleration scenario.

When studying acceleration at a CME-driven shock there many ways that back-precipitation could take place. The first would involve protons back-precipitating along magnetic field lines that wrap around and intersect the shock front, allowing particles to propagate back to the solar surface without interacting with the turbulent field behind the shock. The second would involve protons accelerated at the flanks of the shock. These protons would have shorter propagation distances than protons released at the nose of the shock. However, the highest energy particles, like those that produce the  $\gamma$ -rays during LDGRFs, are believed to be mostly accelerated around the nose of the shock, as the shock speed and compression ratio decrease quickly at the flanks resulting in a reduced acceleration efficiency (e.g. Zank et al. (2006); Hu et al. (2017)). The third method of back-precipitation would involve protons accelerated by the shock back toward the Sun and their subsequent propagation through the turbulent, highly diffusive down stream region behind the shock. This would require them to overcome the outward plasma flow within the CME.

In this paper we study the back-precipitation of energetic protons by simulating their transport from CME-shock heights back to the solar surface, by means of a full-orbit test particle code. We analyse how magnetic mirroring influences this process as a function of shock height and scattering mean free path. We also examine how the position of the  $\gamma$ -ray emission region on the solar surface varies with time. In addition to investigating the general back-precipitation process in an idealised situation, we consider specific LDGRF events in sections 2 and 5, showing how the speed of the CME-shock influences the total precipitation fraction.

In section 2 we analyse shock heights as a function of time for typical CMEs observed during LDGRF events. In section 3 an analytical expression is presented that describes the mirror point radius of non-scattered protons in the Parker spiral magnetic field and mirror point radii are determined from test particle simulations in the

presence of scattering. The results from these simulations, including the effects of pitch angle scattering and radial height of injection on the fraction of successfully precipitating protons, for single injections are discussed in section 4. In section 5 we then estimate the total fraction of precipitating protons for individual LDGRF events. The temporal evolution of the location of  $\gamma$ -ray emission on the solar surface is discussed in section 6, and section 7 presents discussion and conclusions.

## 2. SHOCK HEIGHTS AT TIMES OF $\gamma$ -RAY EMISSION

Winter et al. (2018) showed that, in general, longer duration  $\gamma$ -ray events tend to be associated with faster CMEs. Here we considered a subset of events from the Winter et al. (2018) study with a  $>2$  hour duration. These events are listed and discussed further in section 5 (see Table 2).

The 8 LDGRF events are associated with CMEs that have plane of sky speeds ranging from 950 to 2684 km s<sup>-1</sup> based on the SOHO/LASCO CME catalog ([https://cdaw.gsfc.nasa.gov/CME\\_list/](https://cdaw.gsfc.nasa.gov/CME_list/)). For the CME-driven shock to be the dominant source of the  $\gamma$ -ray emission,  $>300$  MeV protons must be able to propagate back to the solar surface from the position of the shock efficiently. Therefore, it is useful to gain an approximate grasp of the shock positions over the duration of the detected  $\gamma$ -ray emission. In Figure 1 the shock positions at the peak (circles) and end (squares) times for the  $\gamma$ -ray emission are plotted. We used data from Table 3 and the corresponding plots in Appendix C of Share et al. (2018) for the times of the peak of the emission and for the end times of the events we used data from Table 1 of Winter et al. (2018). To a first approximation, we assume that the shock height and speed coincide with those of the associated CME. Within  $30 R_{\odot}$  we use the positions determined using the linear fit in the SOHO/LASCO CME catalog. The shaded wedges in Figure 1 span 500 km s<sup>-1</sup> increments in constant shock speed from 500 to 3000 km s<sup>-1</sup>.

When estimating the position of the shock at the peak and end times of detected  $\gamma$ -ray emission, we take into account deceleration of the shock front in interplanetary space. We use the empirical expression determined by Gopalswamy et al. (2001) for constant shock acceleration (or deceleration) during the propagation to 1 AU, which is given by:

$$a_{sh} = 2.193 - 0.0054 v_{sh} \quad (1)$$

where  $a_{sh}$  is the acceleration/deceleration of the shock in m s<sup>-2</sup> and  $v_{sh}$  is the shock speed in km s<sup>-1</sup>. According to this equation shocks faster than  $\sim 406$  km

s<sup>-1</sup> tend to decelerate. All the shocks considered here are significantly faster than this and so are expected to decelerate during their propagation. We used Equation 1 to find the approximate positions of the shock at the time of peak and end  $\gamma$ -ray emission for the 8 LDGRF events when they are located beyond the LASCO C3 field of view of  $30 R_{\odot}$ . We assume the shock propagates perfectly radially.

Figure 1 shows that if the CME-driven shock is the source of the  $\gamma$ -ray emission in LDGRFs,  $>300$  MeV protons need to back-precipitate to the solar surface from large distances. This is clear when considering the 2012 March 7th event, which was associated with two fast CMEs erupting in rapid succession, with 2684 km s<sup>-1</sup> and 1825 km s<sup>-1</sup> plane-of-sky speeds respectively. Data points for both CMEs are plotted in Figure 1. While the absence of interplanetary type III radio emissions during the second, much slower CME eruption suggests that it was unlikely associated with the SEP event (see Richardson et al. (2014)). However, a direct contribution to particle acceleration cannot be ruled out, so both CMEs are considered here. The  $\gamma$ -ray emission associated with this event was observed for approximately 19.5 hours, so at the end time of detected  $\gamma$ -ray emission these shocks would be located at  $\sim 242 R_{\odot}$  and  $\sim 155 R_{\odot}$  respectively.

For the 8 LDGRF events plotted in Figure 1, the average event duration is 7.25 hours and the mean position of the shock at the end time is  $\sim 86 R_{\odot}$  (including both shocks that originated on 2012-03-07).

Note that in Figure 1 the shock positions at the time of peak observed  $\gamma$ -ray emission differ greatly, indicating that the peak injection of protons by the shock does not occur at the same spatial position and likely relies on other factors affecting the acceleration efficiency, such as the shock speed and geometry, the coronal magnetic field strength and the presence of seed particle populations and pre-existing turbulence.

## 3. DERIVATION OF THE MIRROR POINT RADIUS

Due to magnetic mirror effect, as charged particles propagate toward the Sun, into a region of greater magnetic field strength, their pitch angle is shifted toward 90°. The particle's motion is slowed in the direction parallel to the magnetic field line and the component of velocity perpendicular to the field,  $v_{\perp}$ , increases. At the mirror point the component of velocity parallel to the field,  $v_{\parallel}$ , goes to zero and the direction of motion reverses.

For a Parker spiral magnetic field, (see e.g. Equation 2 of Marsh et al. (2015)) and scatter-free particle propaga-

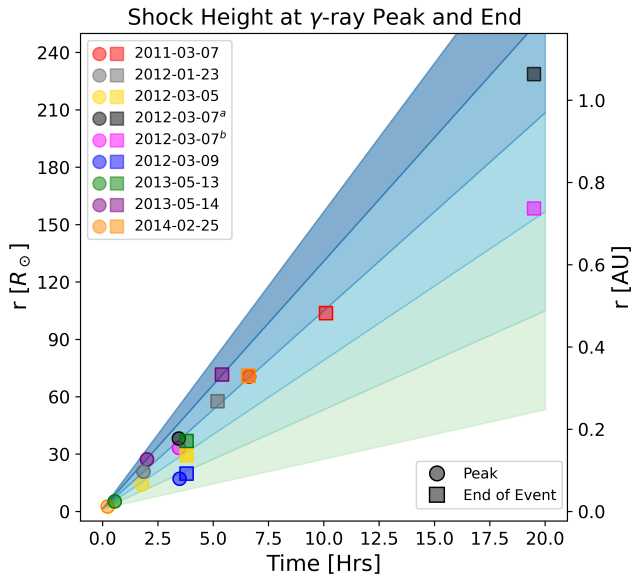


**Figure 1.** The shock positions (radial distance from formation position at  $1.43 R_{\odot}$  from the centre of the Sun) of CME-driven shocks associated with LDGRFs at the peak times (*circles*) and end times (*squares*) of detected  $\gamma$ -ray emission. Constant deceleration is assumed during propagation, as given by Equation 1, and initial plane of sky speeds are taken from Table 1 of Winter et al. (2018). Each shaded wedge spans  $500 \text{ km s}^{-1}$  increments in radial shock speed between  $500$  and  $3000 \text{ km s}^{-1}$ . For the 2012-03-07 event we show two sets of radial positions for two different CME-driven shocks that day: 2012-03-07<sup>a</sup> is the earlier, faster CME with a speed of  $2684 \text{ km s}^{-1}$  and 2012-03-07<sup>b</sup> is the second, slower CME with a speed  $1825 \text{ km s}^{-1}$  (both speeds from the SOHO/LASCO CME catalog).

tion, it is possible to derive an expression for the radial position of the mirror point,  $r_{mp}$ , analytically given by:

$$r_{mp} = \frac{B_0}{B_i} r_0 \sin \alpha_i \left[ \frac{r_0^2 \sin^2 \alpha_i}{2a^2} + \sqrt{\frac{r_0^4 \sin^4 \alpha_i}{4a^4} + \frac{B_i^2}{B_0^2}} \right]^{1/2} \quad (2)$$

where  $B_0$  is the magnetic field strength at a fixed reference radial distance  $r_0$  (we choose  $r_0 = 1 R_{\odot}$ ),  $B_i$  is the magnetic field strength at the starting location of the particle, at radial distance  $r_i$  from the centre of the Sun,  $\alpha_i$  is the initial pitch angle at  $r_i$  and  $a$  is a function of initial colatitude  $\theta$  given by  $a = v_{sw}/(\Omega \sin \theta)$ , with  $v_{sw}$  as the uniform solar wind speed and  $\Omega$  as the sidereal solar rotation rate.

Note that all terms in Equation 2 involving the strength of the magnetic field are ratios at two different radial positions. Hence the mirror point radius under scatter-free conditions is independent of the magnetic field strength and depends only on the  $B_1/B_0$  ratio.

### 3.1. The test particle simulation

To model the propagation of the energetic protons toward the solar surface we used a full-orbit test particle code, specifically an adapted version of the code used by Marsh et al. (2013). We considered a 300 MeV mono-energetic proton population, instantaneously injected into a  $8^\circ \times 8^\circ$  region, in longitude and latitude, centred on  $0^\circ \times 0^\circ$  at a user specified radial height (the injection radius,  $r_i$ ) above the solar surface. Note that acceleration at the shock is not modelled. The protons' positions within the injection region are random and the population is isotropic about a hemisphere in velocity space at the initial time, corresponding to only sunward propagating protons. We use a small injection region that models only a small portion of the shock. However, this small region placed at different heights can model different parts of the shock thereby allowing descriptions of different possible acceleration sites to be considered (i.e. acceleration at the flanks of the shock or nearer the nose depending on the radial height of the injection region). The equation of motion (see Marsh et al. (2013) equation 3) for each proton is integrated to determine its trajectory.

The magnetic field in the model is a Parker spiral field as in Marsh et al. (2013). This is known to be a good approximation only down to  $r \sim 2.5 R_{\odot}$  (the nominal source surface), below which a more complex coronal magnetic field is present. Here potential field source surface models are typically used, while beyond the source surface the average magnetic field is thought to follow a Parker spiral geometry (Owens & Forsyth 2013). We chose to consider a Parker spiral in this initial investigation to identify the key processes and because in many events CME-shock would be injecting particles at heights much larger than the source surface.

We consider a unipolar Parker spiral magnetic field with positive magnetic polarity (i.e. outward pointing) using the same parameters as in Marsh et al. (2013). Hence, for this magnetic geometry pitch angles in the range of  $90^\circ < \alpha \leq 180^\circ$  correspond to sunward propagating particles.

The effect of magnetic turbulence is described as pitch angle scattering. The intensity of the scattering is determined by the mean free path,  $\lambda$ . In our simulations scattering events are Poisson distributed temporally with the average scattering time defined by  $t_{scat} = \lambda/v$ , where  $v$  is the particle's velocity (Marsh et al. 2013). During a scattering event the particle's velocity vector is randomly reassigned to another point on a sphere in velocity space (a full discussion of the scattering model can be found in Dalla et al. (2020)), thereby changing its direction of motion. Each simulation propagates parti-

cles through the field considering a constant  $\lambda$ . To investigate the possible shock source scenario, we ran a number of simulations that model the propagation of protons over 24 hours and involved injection regions located at radial positions in the range  $r_i = 5 R_\odot$  to  $r_i = 70 R_\odot$  and scattering conditions in the range  $\lambda = 0.0025$  AU to  $\lambda = 1.0$  AU.

For the protons to go on to produce  $\gamma$ -rays they must reach sufficiently dense regions of the solar atmosphere, such as the lower chromosphere or upper photosphere at  $\sim 1 R_\odot$  (Share et al. 2018; Winter et al. 2018). The test particle code therefore records the time and the associated particle parameters when a particle crosses the  $1 R_\odot$  boundary from larger distances. Particles that cross this boundary are assumed to be absorbed and are no longer propagated.

### 3.2. Mirroring Protons

The mirroring process as derived from our test particle code can be seen in Figure 2, where the radial distance ( $r$ , top panels), heliographic longitude ( $\phi$ , middle panels) and the pitch angle ( $\alpha$ , bottom panels) are displayed for the first 5 minutes of propagation for particles in two different simulations. The left panels are for a particle that propagated scatter-free and the right panels are for a proton in a simulation with a scattering mean free path of  $\lambda = 0.1$  AU. In both simulations the protons were injected at  $r_i = 20R_\odot$ . Scattering produces an abrupt change in trajectory by reassigning the velocity vector of the particle (at  $t \sim 3.5$  minutes and  $t \sim 4$  minutes in the right panels of Figure 2), altering the pitch angle of the particle. The changes in longitudinal position of the proton are due to drifts that occur as the proton propagates through the Interplanetary Magnetic Field (Dalla et al. 2013), the corotation of the system and a small curvature of the Parker Spiral. Adiabatic deceleration is negligible over the timescales depicted in Figure 2.

For each proton injected into the simulation the mirror point was determined by identifying the minimum radial distance the particle reached. Figure 3 shows the mirror point radius,  $r_{mp}$  versus initial pitch angle  $\alpha_i$  for three populations of protons injected at  $r_i = 10, 20$  and  $30 R_\odot$ . For clarity, only a subset of data points (1.5% of the 50000 calculated mirror point radii) are plotted. The purple, orange and green curved dashed lines give the scatter-free analytical value of  $r_{mp}$ , according to Equation 2. A number of data points are found to lie along these lines, corresponding to protons that did not scatter in the simulation, validating our code and methodology for deriving  $r_{mp}$ . The blue dashed line at  $1 R_\odot$  displays the height in the solar atmosphere that the protons must reach to go on to generate  $\gamma$ -rays. Data points not along

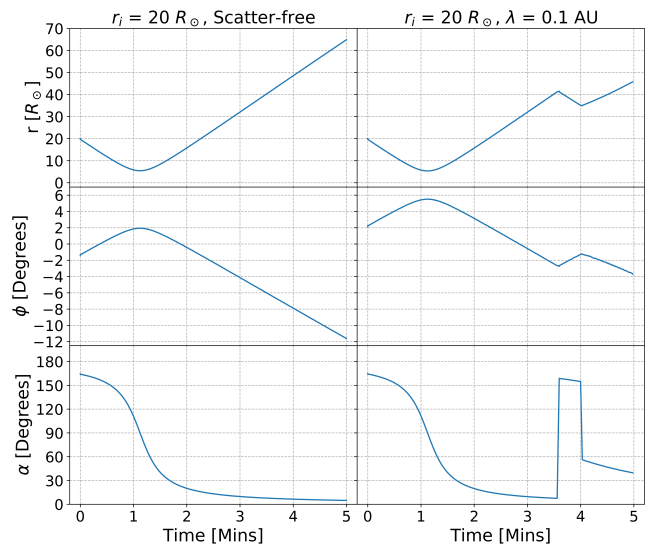


**Figure 2.** The radial position ( $r$ ), heliographic longitude ( $\phi$ ) and pitch angle ( $\alpha$ ) of two 300 MeV protons for the first 5 minutes of two simulations. The left column is for a scatter-free simulation, the right column is for a proton from a simulation with a scattering mean free path of  $\lambda = 0.1$  AU. Both simulations had injection at  $r_i = 20R_\odot$ . Two scattering events occur in the right hand side panels at  $\sim 3.5$  and  $\sim 4$  minutes.

the curved dashed lines correspond to protons that experienced scattering.

In Figure 3 there are a number of green circles and yellow squares close to or below the  $1 R_\odot$  blue dashed line; these protons would be candidates to go on to produce  $\gamma$ -rays. It is clear from Figure 3 that they are a small fraction of the population. In the scatter-free case only a very small proportion of the injected pitch angle distribution (particles with  $\alpha_i$  close to  $180^\circ$ ) can penetrate deep enough into the solar atmosphere to reach the solar surface, while for the scattering case particles across the pitch angle distribution can also reach the solar surface if scattered favourably.

As can be seen from Figure 3, scattering allows the possibility for protons to propagate deeper into the solar atmosphere than they would have in scatter-free conditions (indicated by the points below the corresponding dashed line). These protons' velocity vectors have been scattered such that their pitch angles have shifted toward  $180^\circ$  (i.e. more field aligned). However, there are also a number of points above the scatter-free prediction, which have undergone a scattering event that re-assigned their velocity vectors such that their pitch angles were shifted closer to  $90^\circ$  (or the particle was reflected by the scattering event), resulting in the proton mirroring further from the solar surface than it would have under scatter-free conditions. This raises the question

whether scattering primarily helps or hinders protons in their back-precipitation to the photosphere. This is addressed in section 4.2.

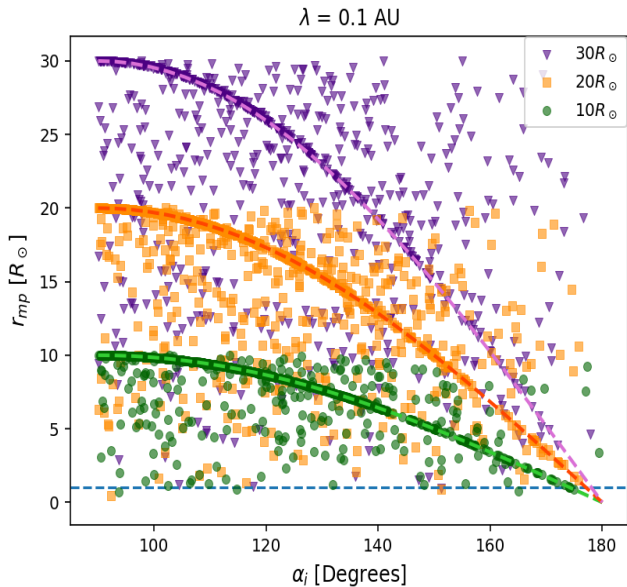


**Figure 3.** The mirror point radius,  $r_{mp}$ , versus particle initial pitch angle,  $\alpha_i$  for simulations with injections at  $10 R_\odot$  (green circles),  $20 R_\odot$  (orange squares) and  $30 R_\odot$  (purple triangles) with  $\lambda = 0.1$  AU. The green, orange and purple dashed lines show the analytical, scatter-free mirror point radius, given by Equation 2. The horizontal blue dashed line denotes the required depth in the solar atmosphere the protons must reach to generate  $\gamma$ -rays ( $1 R_\odot$ ).

#### 4. PRECIPITATION FRACTIONS

We indicate as  $N_p$  the number of protons that successfully precipitate to the precipitation radius  $r_p$  within a simulation and we calculate the precipitation fraction,  $P$  (percentage of the injected population that reach  $r_p$  for injection at height  $r_i$  over the full simulation time of 24 hours). Unless otherwise specified we study precipitation to a precipitation radius of  $r_p = 1 R_\odot$ . Table 1 gives values of  $N_p$  and  $P$  for our simulations.

##### 4.1. Dependence of $P$ on injection height

Figure 4 shows  $P$  versus  $r_i$  for 11 simulations that injected 5 million protons and propagated them under scattering conditions described by  $\lambda = 0.1$  AU, with simulated propagation for 24 hours. Here one can see that  $P$  decreases with increasing radial distance of the injection region. This is due to the stronger magnetic mirror effect for larger  $r_i$ , caused by the greater change in magnetic field strength over the proton’s propagation to the photosphere.

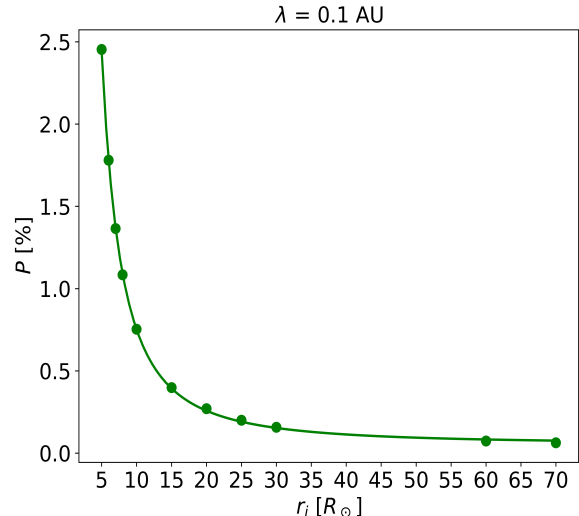


**Figure 4.** Precipitation fraction ( $P$ ) versus radial position of injection ( $r_i$ ) for scattering described by a scattering mean free path  $\lambda = 0.1$  AU. The points have been fitted with the line  $P(r_i) = 41.814 (r_i/R_\odot)^{-1.777} + 0.053$  %.

The radial dependence of the precipitation fraction follows a power law:

$$P(r_i) = 41.814 \left( \frac{r_i}{R_\odot} \right)^{-1.777} + 0.053 \text{ \%} \quad (3)$$

for protons travelling in a turbulent magnetic field described by  $\lambda = 0.1$  AU and  $r_i$  in solar radii. As the shock propagates from 5 to  $70 R_\odot$  the precipitation drops from 2.454% to 0.063%. This corresponds to a drop in the number of protons reaching the solar surface by a factor of  $\sim 39$  assuming the same number of protons are accelerated by the shock at instances of particle acceleration over the radial distances shown in Figure 4. This, however, is an unlikely circumstance because the number of protons accelerated by the shock should change depending on the evolution of the shock and the proton density of intercepted ambient solar wind.

##### 4.2. Dependence of $P$ on $\lambda$

The left panel of Figure 5 shows  $P$  versus  $\lambda$  for simulations that have a common injection region at  $r_i = 20 R_\odot$ . We consider precipitation down to two precipitation radii:  $r_p = 1.0 R_\odot$  and  $r_p = 2.5 R_\odot$ , with the latter representing the height of the source surface. The right panel displays the precipitation fraction versus scattering mean free path for simulations with injection at  $70 R_\odot$  for  $r_p = 1.0 R_\odot$ . From the left panel of Figure 5 we can tell that increased scattering (reduced  $\lambda$ ) aids the protons in their propagation to the solar surface against the magnetic mirror effect. The dependence of the precipitation fraction for  $r_p = 1 R_\odot$  on the scattering mean

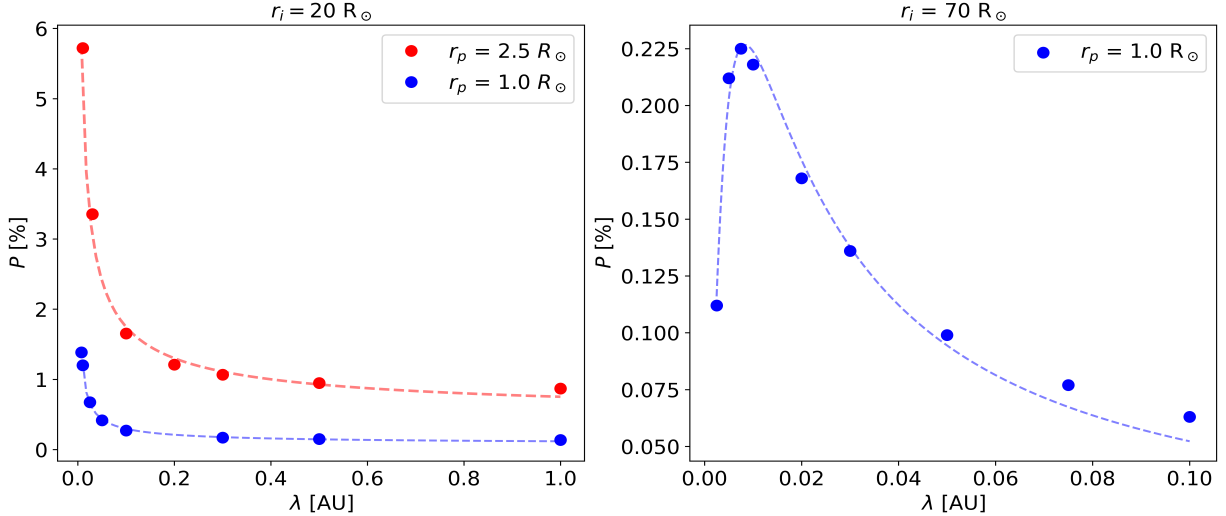


**Figure 5.** Left panel: Precipitation fraction ( $P$ ) versus scattering mean free path  $\lambda$  for  $r_p = 1 R_\odot$  (blue points) and  $r_p = 2.5 R_\odot$  (red points) from simulations over a 24 hour period that were injected at a height of  $r_i = 20 R_\odot$ ,  $\lambda$  ranges from  $\lambda = 0.0075$  AU ( $\sim 1.6 R_\odot$ ) to  $\lambda = 1.0$  AU. The  $r_p = 1 R_\odot$  points are fitted with the curve  $P = 0.046(\lambda/\text{AU})^{-0.690} + 0.072$  % and the  $r_p = 2.5 R_\odot$  points are fitted with the curve  $P = 0.344(\lambda/\text{AU})^{-0.596} + 0.408$  %. Right panel:  $P$  versus the  $\lambda$  for injections at  $70 R_\odot$  for  $r_p = 1 R_\odot$ . Scattering mean free paths range from  $\lambda = 0.0025$  AU to  $\lambda = 0.1$  AU. The points are fit with the curve  $P = (0.006/(\lambda + 0.01)) \exp\{(0.009/(\lambda + 0.01)) - ((\lambda + 0.01)/4.63 \times 10^8)\}$  %.

free path follows a power law:

$$P(\lambda) = 0.046 \left( \frac{\lambda}{\text{AU}} \right)^{-0.690} + 0.072\% \quad (4)$$

for injection at a radial height  $r_i = 20 R_\odot$  and  $\lambda$  in AU.  $P$  increases from 0.138% to 1.384% going from  $\lambda = 1.0$  to 0.0075 AU for  $r_p = 1.0 R_\odot$ . Following this trend, to increase  $P$  further would require very small scattering mean free paths for  $r_i = 20 R_\odot$ , which are computationally expensive with our code and are unrealistic for solar energetic particles. However it is possible to study the qualitative behaviour at small  $\lambda$  by choosing  $r_i = 70 R_\odot$  (right panel of Figure 5). Here one can see that as  $\lambda$  is reduced  $P$  reaches a peak value and then starts decreasing. This is due to particles being easily carried away by the advection of the solar wind. Figure 5 shows that the scattering conditions that yield peak precipitation fractions change depending on the radial position of the injection. To yield peak precipitation fractions particles must be scattered often enough so that the likelihood of scattering into the loss cone is maximum. However, continuing to reduce  $\lambda$  will disrupt the latter process. For particles injected closer to the solar surface this requires a smaller  $\lambda$ . To maintain peak precipitation efficiency would require an increasing scattering mean free path with increasing radial distance of the shock.

In addition to modelling back-precipitation to  $r_p = 1 R_\odot$ , in Figure 5 (left panel) we consider also a precipitation radius  $r_p = 2.5 R_\odot$ , corresponding to the height of the source surface and, roughly, to the radial distance

where the highest energy particles associated with the so called Ground Level Enhancements (GLEs) are released from the shock (Reames 2009; Gopalswamy et al. 2013a).

The left panel of Figure 5 shows that for  $r_p = 2.5 R_\odot$  there is only a few percent increase in the precipitation fraction, and these protons still need to propagate a further  $\sim 1.5 R_\odot$  to produce  $\gamma$ -rays. Therefore, despite the simplicity of our model, we can speculate that the precipitation fractions are expected to be similarly small even accounting for more complex magnetic structures in the corona.

Most of the protons that reach the solar surface do so early in time. This is especially important for simulations with large  $\lambda$  (low numbers of scattering events) as the protons that precipitate early represent a very large percentage of the total number of successfully precipitating protons. We define  $F_{10mins}$  as the percentage of the total precipitating protons over the full simulation (24 hours),  $N_p$ , that precipitate in the first 10 minutes. The last column in Table 1 gives  $F_{10mins}$  for our simulations. For a simulation with  $r_i = 20 R_\odot$  and  $\lambda = 0.1$  AU the proportion of the protons that precipitate over the 24 hour simulation that do so in the first 10 minutes is  $F_{10mins} = \sim 76\%$ . For the same injection location, when  $\lambda = 0.01$  AU, this drops dramatically to  $F_{10mins} = \sim 26\%$ . However, a greater number of protons than the  $\lambda = 0.1$  AU simulation reach the solar surface over the first 10 minutes for the  $\lambda = 0.01$  AU simulation because precipitation is more efficient under greater scattering

$r_i$ [ $R_\odot$ ]	$\lambda$ [AU]	$N_p$	$P$ [%]	$F_{10min}$ [%]
5	0.1	122688	2.454	97.4
6	0.1	89039	1.781	96.5
7	0.1	68235	1.365	95.2
8	0.1	54195	1.084	94.1
10	0.1	37653	0.753	91.5
15	0.1	19935	0.399	84.0
20	0.1	13496	0.270	76.2
25	0.1	10017	0.200	67.8
30	0.1	7863	0.157	60.5
60	0.1	3667	0.073	23.4
70	0.1	3156	0.063	15.8
20	0.0075	69192	1.384	19.0
20	0.01	60038	1.201	26.2
20	0.025	33710	0.674	49.3
20	0.05	20809	0.416	64.1
20	0.3	8540	0.171	88.9
20	0.5	7539	0.151	92.5
20	1.0	6881	0.138	96.4
20	Scatter-Free	6224	0.124	100.0
70	0.0025	5621	0.112	0.0
70	0.0050	10617	0.212	0.0
70	0.0075	11274	0.225	0.0
70	0.01	10904	0.218	0.0
70	0.02	8384	0.168	0.1
70	0.03	6790	0.136	1.0
70	0.05	4944	0.099	5.0
70	0.075	3866	0.077	10.6

**Table 1.** Precipitation fractions for our simulations. Columns are: (From left to right) The radial height of the shock at particle injection ( $r_i$ ), the parallel scattering mean free path ( $\lambda$ ), the number of precipitating protons that reach  $1 R_\odot$  over the full 24 hour simulation ( $N_p$ ), the precipitation fraction ( $P$ ), and the percentage of the precipitating protons that reach the solar surface in the first 10 minutes after injection ( $F_{10min}$ ). All simulations injected a 300 MeV mono-energetic proton population consisting of 5 million protons into a  $8^\circ \times 8^\circ$  injection region.

conditions. As expected more turbulent magnetic fields lead to smaller  $F_{10min}$  values as protons are slowed due to more frequent scattering events. Simulations with injections close to the solar surface have high  $F_{10mins}$  values, for instance  $F_{10min} = 97.438\%$  for a simulation with,  $r_i = 5 R_\odot$ ,  $\lambda = 0.1$  AU. This percentage decreases with increasing radial position of the injection region, (see Table 1).

The precipitation rate ( $P_{rate}$ , the number of protons precipitating per second) can be seen in Figure 6 for the  $\lambda = 0.1$  AU and  $\lambda = 0.01$  AU,  $r_i = 20R_\odot$  simulations. In Figure 6 the simulation with  $\lambda = 0.1$  AU has a spike

at the beginning due to non-scattered protons propagating to the solar surface. These protons will have the largest component of their velocity anti-parallel to the magnetic field line ( $\alpha$  close to  $180^\circ$ , largest  $v_{\parallel}$ ) and so reach the solar surface early in time. The  $\lambda = 0.01$  AU simulation does not show a spike as most protons are scattered at least once before reaching  $1 R_\odot$  and will either propagate to the photosphere in a time later than the scatter-free propagation time or they may not reach the solar surface at all. Scattering will only act to slow the protons with initial pitch angles close to  $180^\circ$  because they have the most field aligned initial velocities (i.e. they propagate fastest along the field out of the population). Therefore, scattering will tend to lengthen the duration of the precipitation from a single injection at the shock. As a result these conditions allow a larger number of protons to reach the solar surface in the first 10 minutes than the  $\lambda = 0.1$  AU simulation, by enabling particles that would not reach the solar surface to be scattered into the loss-cone. Therefore, increased scattering yields more efficient time-extended precipitation than in the lower scattering case, for particles injected at around  $20 R_\odot$ . Hence during the first 10 minutes the  $\lambda = 0.01$  AU simulation would produce a greater number of  $\gamma$ -rays than the  $\lambda = 0.1$  AU case. However, the  $\lambda = 0.1$  AU case would initially produce a greater number of  $\gamma$ -rays (due to the initial spike) but would decay much faster than the  $\lambda = 0.01$  AU case. This is clearly visible in Figure 6.

It is important to mention that protons are able to propagate to the solar surface regardless of the level of the scattering, for the values of  $\lambda$  that we considered. However, the proportion of the injected population that successfully precipitate is altered significantly by the scattering conditions, as seen in Table 1 and Figure 5.

Assuming that the shock accelerates protons continuously over its propagation away from the Sun, the shape of the  $\gamma$ -ray profile produced will be determined by the superposition of the histograms of precipitation rate (see Figure 6) for each instance of particle acceleration shifted in time in accordance with the shock position at the times of injection. For the low-scattering case the spikes from non-scattered protons from each instance of particle acceleration will form the shape of the  $\gamma$ -ray profile, with minimal contribution from the protons that precipitate later due to the rapid decay in precipitation rate. Therefore, in this case the shape of the  $\gamma$ -ray profile is highly dependent on the pitch angle distribution at injection. To achieve a smooth  $\gamma$ -ray profile without a rapid decay as observed by *Fermi*/LAT, the shock must continuously accelerate particles. On the other hand, for

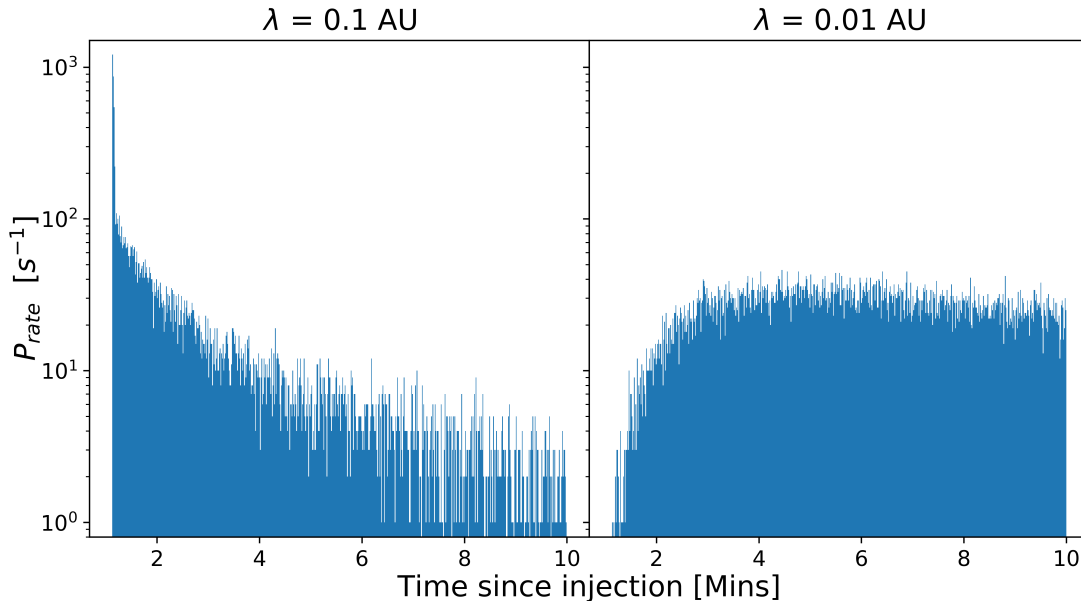


**Figure 6.** Histogram of the precipitation rate ( $P_{rate}$ , the number of 300 MeV protons reaching the solar surface per second) over the first 10 minutes for simulations from single injections at an injection radii of  $r_i = 20 R_\odot$  with scattering mean free paths of 0.1 AU (left) and 0.01 AU (right).

protons accelerated in a high turbulence magnetic field the precipitation rate is characterised by a gradual increase and slow sustained decay. This large decay phase leads to a  $\gamma$ -ray profile composed of significant contributions from multiple instances of particle acceleration. Therefore in high scattering conditions the shape of the  $\gamma$ -ray profile does not depend on the distribution of the injection pitch angles, as the scattering allows particles from across the pitch angle distribution to precipitate over extended times. In the case of a highly turbulent magnetic field, particle acceleration at the shock can be much more sporadic than the low-scattering case as the sustained decay from previous injections will continue to produce a smooth  $\gamma$ -ray profile.

## 5. TOTAL PRECIPITATION FRACTION

Each of the LDGRF events in Figure 1 have associated CMEs with different speeds, where the shocks travel from  $r = 5$  to  $r = 70R_\odot$  over different time frames. Each CME-driven shock associated with the LDGRF event experiences a change in precipitation fraction, as shown in Figure 4, over timescales that are specific to each event. By extrapolating from the relation in Figure 4 (Equation 3), we can approximate the total precipitation fraction for each shock associated with the LDGRF events plotted in Figure 1.

The following relation can be used to determine the total precipitation fraction,  $\bar{P}$ , of a specific event:

$$\bar{P} = \frac{\int_{r_{ini}}^{r_{fin}} N(r_i)P(r_i) dr_i}{\int_{r_{ini}}^{r_{fin}} N(r_i) dr_i} \quad (5)$$

where  $r_{ini}$  is the radial position of the shock when particle acceleration begins,  $r_{fin}$  is the radial position of the shock when particle acceleration ends,  $P(r_i)$  is the function describing the radial evolution of the precipitation fraction displayed by the fit in Figure 4 (Equation 3), and  $N(r_i)$  is an injection function that describes the number of injected particles as a function of radial distance. Hence, the numerator is the total number of precipitating protons over an event and the denominator is the total number of injected protons. For a constant injection function this simplifies to,

$$\bar{P} = \frac{1}{r_{fin} - r_{ini}} \left( \int_{r_{ini}}^{r_{fin}} P(r_i) dr_i \right) \quad (6)$$

To calculate  $\bar{P}$  we need to specify  $r_{ini}$  and  $r_{fin}$  for each event. We assume that particle acceleration begins at the radial position of the formation of the shock. Gopalswamy et al. (2013b) determined a mean shock formation height of  $r_{ini} = 1.43 R_\odot$  which we use here for all shocks. We determine  $r_{fin}$  by calculating the shock position at the time when the detected  $\gamma$ -ray emission associated to the event ended (based on  $\gamma$ -ray event durations - see Table 2). The values of  $r_{fin}$ , which were also plotted in Figure 1, are shown in Table 2 and were determined using the plane of sky CME speeds that are provided in

Date	$v_{sh}$ [km s <sup>-1</sup> ]	C2 Time [UT]	D [Hrs]	$r_{fin}$ [ $R_{\odot}$ ]	$\bar{P}$ [%]
2011-03-07	2125	20:00:05	10.1	103.627	0.438
2012-01-23	2175	04:00:05	5.2	57.525	0.739
2012-03-05	1531	04:00:05	3.6	29.205	1.380
2012-03-07 <sup>a</sup>	2684	00:24:06	19.5	228.596	0.230
2012-03-07 <sup>b</sup>	1825	01:30:24	19.5	158.378	0.307
2012-03-09	950	04:26:09	3.8	19.708	1.992
2013-05-13	1850	16:07:55	3.8	36.744	1.115
2013-05-14	2625	01:25:51	5.4	71.496	0.607
2014-02-25	2147	01:25:50	6.6	70.915	0.612

**Table 2.** Total precipitation fractions over the full duration of the 8 LDGRF events plotted in Figure 1. Columns are: (From left to right) The date of the LDGRF event, the speed of the shock associated with the CME ( $v_{sh}$ ), the time of CME first appearance in the LASCO C2 field of view; obtained from the SOHO/LASCO CME catalog, the duration of the detected  $\gamma$ -ray emission from the *Fermi* LAT instrument (D); obtained from Table 1 of Winter et al. (2018), the position of the shock at the end time of detected  $\gamma$ -ray emission of the event ( $r_{fin}$ ); determined using Equation 1, and the total precipitation percentage ( $\bar{P}$ ) over the propagation of the shock from  $r_{ini}$  ( $= 1.43 R_{\odot}$ ) to  $r_{fin}$ ; determined using Equation 6. The total precipitation fraction considers the fact that the instantaneous precipitation fraction decreases with the radial dependence of Figure 4 and assumes the scattering can be described by  $\lambda = 0.1$  AU. There were two CMEs associated with the 2012-03-07 event, consequently 2 shocks were formed. CME *a* occurred first and is associated with the X5.4 flare; which entered the LASCO C2 field of view at 00:24:06 UT and the second CME, *b*, is linked with the X1.3 flare; which entered the LASCO C2 field of view at 01:30:24 UT.

Table 1 of Winter et al. (2018) (SOHO/LASCO speeds, given in the second column of Table 2) - see section 2. We calculate the total precipitation fraction for conditions where scattering due to magnetic turbulence can be described by  $\lambda = 0.1$  AU, corresponding to strong scattering. We provide the time of first appearance in the LASCO C2 field of view to identify each shock, in the third column of Table 2. The duration of detected  $\gamma$ -ray emission is also displayed in the fourth column of Table 2.

The values for  $\bar{P}$  we obtained are displayed in the final column of Table 2 for the 8 LDGRF events (9 shocks) displayed in Figure 1. It can be seen here that the total precipitation fractions are extremely small, ranging between 0.230% and 1.992%.

It should be noted that the height at which the shock begins to inject protons ( $r_{ini}$ ) has a large effect on the overall value of  $\bar{P}$  as the precipitation fraction increases dramatically closer to the solar surface. For example if the shock in the 2012-01-23 event formed at  $2.0 R_{\odot}$ , as estimated by Joshi et al. (2013), instead of  $r_{ini} = 1.43 R_{\odot}$  used here, the  $\bar{P}$  for the event would drop to 0.578% from 0.739%. Similarly, Gopalswamy et al. (2013b) computed a  $1.93 R_{\odot}$  shock formation height for the 2011-03-07 event, which would correspond to a decrease in its total precipitation fraction from 0.438% to 0.357%. Note, that here we are still operating under the assumption that particle acceleration begins at the height the shock forms. However, it takes time to accelerate protons to the  $>300$  MeV energies that is required to produce  $\gamma$ -rays and so these  $\bar{P}$  values are overestimates.

The total precipitation fraction of the event,  $\bar{P}$ , becomes substantially smaller if acceleration at the CME-shock continues over larger distances, as can be seen from Table 2 considering the events with the largest values of  $r_{fin}$ . Typically these are the events with either very long durations or very fast shocks or both. Looking at the two shocks associated with the 2012-03-07 event one can see that having a slower shock over the same duration will lead to an increased  $\bar{P}$ . Note that if the proton acceleration occurs at the flanks of the shock this would increase the  $\bar{P}$  as the flanks remain closer to the solar surface than the nose of the shock over the shock's propagation. However, higher energy particles are believed to be more efficiently accelerated over smaller shock region around the nose, while the shock speed and compression ratio decrease quickly at the flanks (Zank et al. 2006; Hu et al. 2017).

The speeds used to calculate the  $\bar{P}$  values are average speeds of the CMEs over the field of view of LASCO ( $30 R_{\odot}$ ). Therefore, closer to the Sun the shocks are likely faster than shown in Table 2, as the speeds in the table are plane of the sky speeds and they underestimate the true space or 3D speeds due to projection effects. This is of particular importance for shocks nearer the central meridian, such as the 2012-03-09 event, which had a flare located at N15 W03, according to the locations given by Winter et al. (2018). Both the consideration of the average shock speed as the initial shock speed and the low initial injection height aim to provide the best opportunity for high precipitation values. However, even

with these assumptions the total precipitation fractions remain very small.

de Nolfo et al. (2019) directly compared the number of protons interacting at the Sun inferred from *Fermi*-LAT  $\gamma$ -ray measurements, and the number of SEP protons at 1 AU obtained by reconstructing the spatial distribution with multi-point spacecraft observations, accounting for both longitudinal and latitudinal magnetic connectivity. Assuming the two populations have a common origin associated with particle shock acceleration, a lower limit on the total precipitation fraction can be calculated. They did so for 14 SEP events, of which 6 are in common with the sample analysed in this work: 2011-03-07, 2012-01-23, 2012-03-07 (*a* and *b*), 2012-03-09 and 2014-02-25. The relatively small value ( $\sim 2.9\%$ ) obtained for the 2014-02-25 event is almost a factor 5 greater than our estimate ( $\sim 0.6\%$ ). In the case of the 2012 March 7-10 events, being impossible to evaluate the individual contributions in terms of SEP intensities at 1 AU, de Nolfo et al. (2019) provided a single precipitation fraction value of  $\sim 18\%$ , which exceeds by at least 9 times the values that we calculated for three CMEs on 2012 March 7 - 9 considered in this work ( $\sim 0.2 - 2.0\%$ ); similar results are expected for the March 10 CME, characterised by an intermediate speed. Finally, for the 2011-03-07 and 2012-01-23 events they reported a  $>90\%$  precipitation fraction, more than two orders of magnitude greater than our predictions ( $\sim 0.4\%$  and  $\sim 0.7\%$ , respectively).

Overall we conclude that while in many events the direct observational comparison between the interacting and SEP populations gives rise to a requirement of large precipitation fractions under the assumption of CME-shock acceleration of both populations (de Nolfo et al. 2019), for the same events our modelling cannot produce them due to the strong effect of magnetic mirroring. This poses a problem for the CME-shock hypothesis for LDGRFs.

So far in this section we have considered  $N(r_i) = \text{constant}$  in Equation 5. Now we consider an injection that varies with height according to the equation:

$$N(r_i) = \frac{1}{(r_i - r_{ini})} \exp\left(\frac{-A}{(r_i - r_{ini})} - \frac{(r_i - r_{ini})}{B}\right) \quad (7)$$

where  $r_{ini}$  is the radial position at which injection starts (assumed to be  $1.43 R_\odot$ ),  $r_i$  is the radial position of the shock and  $A$  and  $B$  are constants that determine the rate of the rise and decay phases respectively and the position of peak injection. This functional form describes a fast rise phase to peak injection, then a turnover and subsequent slow decay, consistent with the fact that both the

shock and magnetic field strength decrease with increasing heliocentric distance, so that energetic particles are efficiently accelerated at earlier times when the shock is closer the Sun. Gopalswamy et al. (2013a) found that the majority of the injections of the high energy particles associated with the solar cycle 23 Ground Level Enhancements were located between  $2.0$  and  $4.0 R_\odot$ . The top left panel of Figure 7 shows  $N(r_i)$  for different values of  $A$  and a constant radial position of peak injection,  $r_{peak} = 5.0 R_\odot$ . The injection functions are normalised, so that the total number of injected particles is the same for different curves. The top right panel of Figure 7 displays the corresponding total precipitation fractions, determined using Equation 5, where each coloured point represents  $\bar{P}$  of the same coloured curve in the top left panel. The bottom left panel displays injection functions with differing  $r_{peak}$  values and the bottom right panel the corresponding  $\bar{P}$  values.

As can be seen in Figure 7, injection functions that inject a larger proportion of the energetic proton population far from the solar surface result in a smaller  $\bar{P}$  than those that inject a large proportion of protons closer to the solar surface. This decrease in  $\bar{P}$  occurs for both increasing radial position of peak injection and extended decay phases of the injection function, and is easily identifiable by comparing the blue and purple injection functions and their corresponding  $\bar{P}$  in Figure 7. The blue and purple injection functions in the top left panel have total precipitation fractions of  $0.587\%$  and  $1.673\%$  respectively. Even though the position of peak injection remains the same the extended decay phase of the blue curve leads to a decrease in  $\bar{P}$ , which is substantial compared with the majority of  $\bar{P}$  values for a constant injection function, like those considered for the LDGRFs in Table 2. Similarly, the injection functions in the bottom left panel of Figure 7 also show a dramatic difference in  $\bar{P}$  with the blue and purple curves corresponding to  $5.920\%$  and  $0.495\%$  respectively. This panel highlights the strong radial dependence of the efficiency of the back-precipitation process as each consecutive injection function results in a broader injection with peak injection occurring further from the Sun, which corresponds to increasingly smaller  $\bar{P}$  values. Interestingly, by comparing the blue curve of the top left panel and the purple curve of the bottom left panel of Figure 7 we can determine that the radial position of the shock at the initial injection of protons,  $r_{ini}$  has a larger effect on the total precipitation fraction than the length of the decay phase of the injection. The purple curve in the bottom left panel begins injecting particles further from the solar surface and with a shorter decay phase than that of the blue curve in the top left panel. Even with

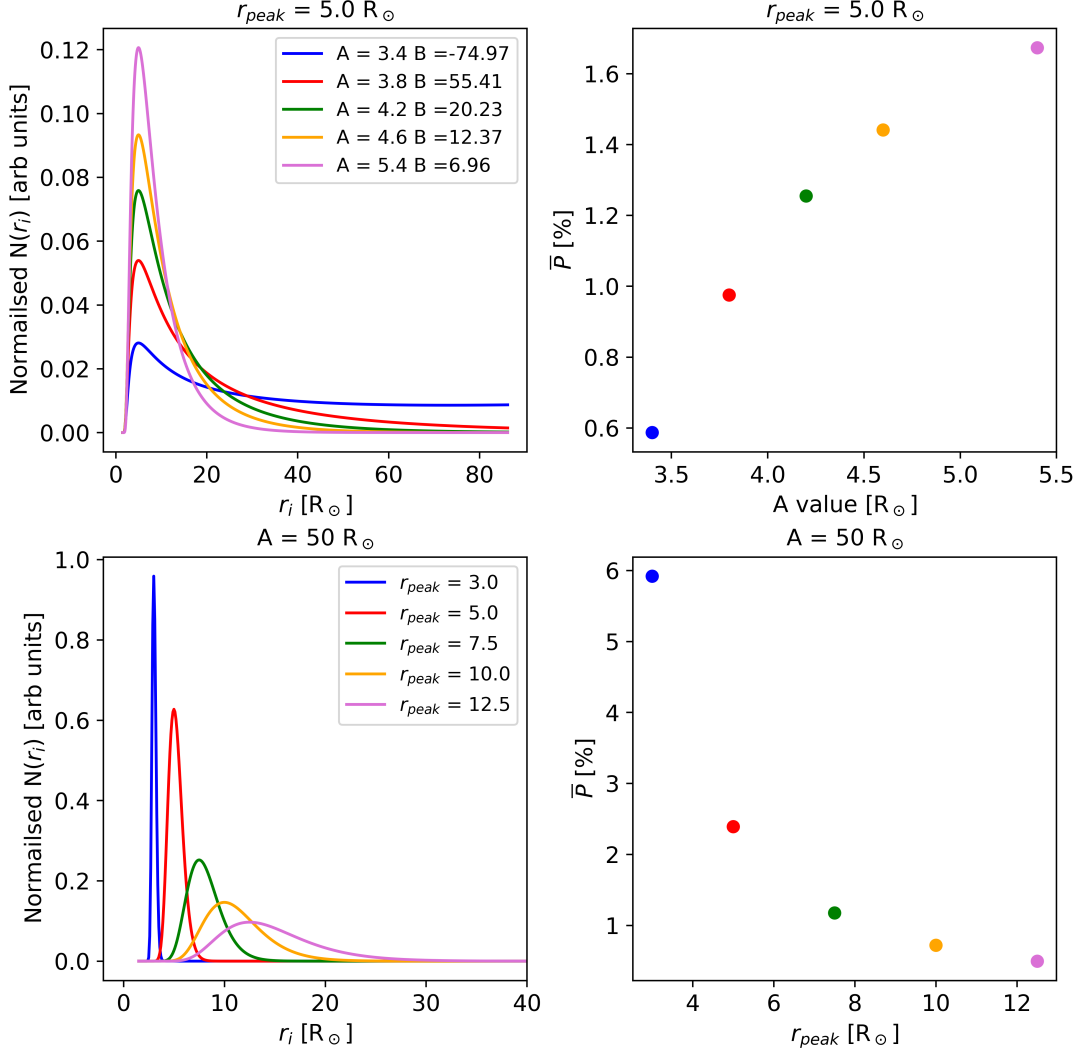


**Figure 7.** The top left panel displays the normalised injection functions with a peak injection at  $5.0 R_\odot$  with differing decay rates versus the radial position of the shock at particle injection over the range  $r_i = 1.43$  (where particle injection is assumed to begin in the calculations above) to  $86.24 R_\odot$  (the average end time position from the shocks in Figure 1). The top right panel shows the corresponding total precipitation fraction ( $\bar{P}$ ) versus the value of the constant  $A$ . Each coloured point in the top right panel represents  $\bar{P}$  for the same coloured curve in the top left panel. The bottom left panel displays the normalised injection functions for  $A = 50 R_\odot$  at different radial positions of peak injection. The bottom right panel displays the corresponding total precipitation fraction to the injections displayed in the bottom left panel, these are displayed by points of the same colours as the curves. Note that since this uses the fit from Figure 4 (Equation 3) this is only applicable for scattering conditions of  $\lambda = 0.1$  AU.

the shorter decay phase the purple curve yielded a total precipitation fraction that was  $\sim 0.1\%$  of the injected population lower than that of the blue curve in the top left panel. Therefore, fast particle acceleration by the shock close to the Sun, leading to a prompt injection, is important to ensuring large total precipitation fractions.

When we calculate total precipitation fraction for our 8 LDGRF events considering an injection function  $N(r_i)$  that is not constant with  $r_i$  we obtain values for  $\bar{P}$  that are larger than those in Table 2 but still overall smaller than 10 %.

## 6. LONGITUDINAL AND LATITUDINAL POSITION OF THE EMISSION REGION

In Figure 8 the locations where the protons crossed the  $1 R_\odot$  boundary are displayed for two particle energies (300 MeV (top panels) and 1 GeV (bottom panels)) and scattering mean free paths of  $\lambda = 0.1$  AU (panels a and c) and  $\lambda = 0.01$  AU (panels b and d) in a coordinate system corotating with the Sun. The red square is the region of the photosphere directly connected to the injection region. All simulations had injections located at  $r_i = 20 R_\odot$ .

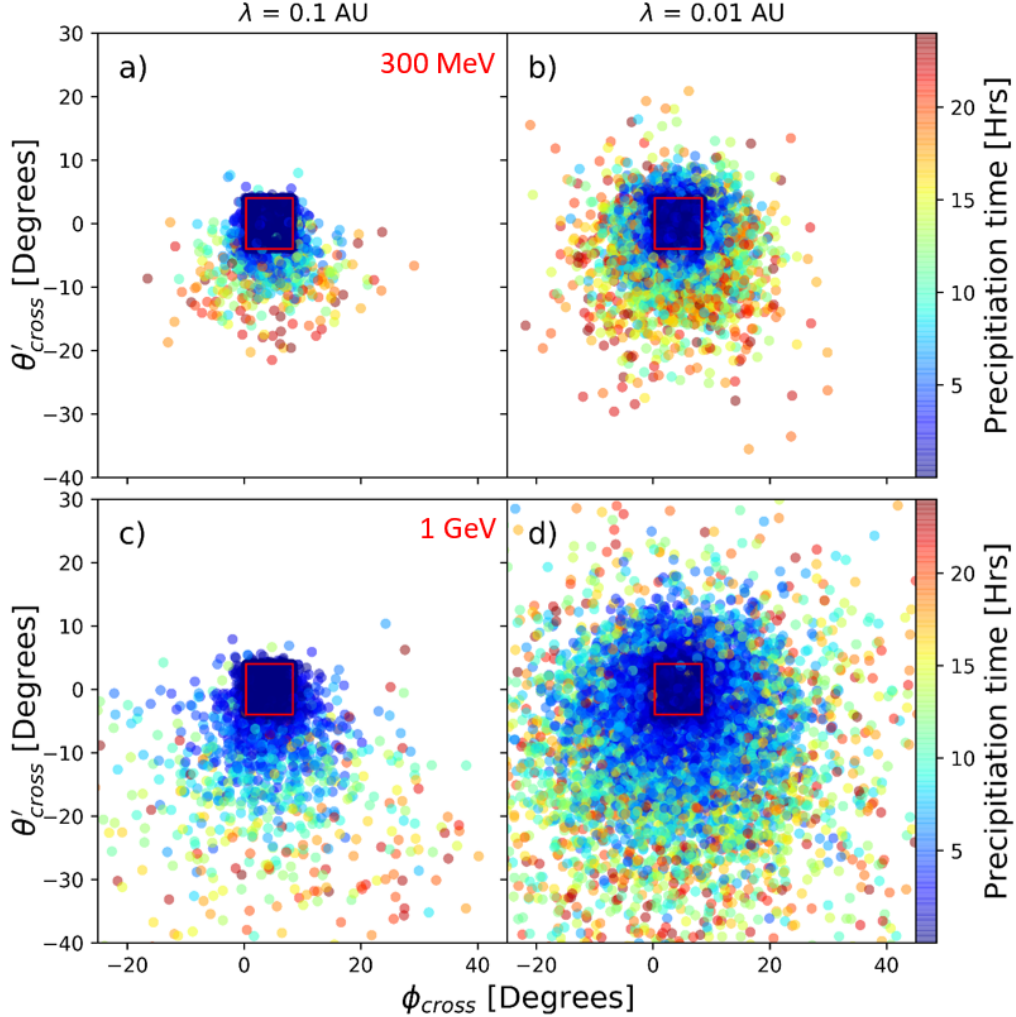


**Figure 8.** The heliographic latitude ( $\theta'_{cross}$ ) and longitude ( $\phi_{cross}$ ) of the energetic protons that reach the solar surface for simulations with; an  $8^\circ \times 8^\circ$  injection region (centred at  $0^\circ, 0^\circ$ ) at a radial distance of  $r_i = 20 R_\odot$  and scattering conditions defined by mean free paths of 0.1 AU (panels a and c) and 0.01 AU (panels b and d). The top two panels (a and b) are for simulations with a 300 MeV mono-energetic proton population, the bottom two panels (c and d) are for simulations with a 1 GeV mono-energetic proton population. The red box denotes the region on the solar surface of the injection region if only propagation along the Parker spiral occurs.

In Figure 8 panels a) and c) there is a systematic drift of the crossing position southwards with time. The same trend is seen in Figure 8 panels b) and d). However, some crossings are also observed northwards of the emission region. The southward drift is due to gradient and curvature drifts associated to the Parker spiral magnetic field (Dalla et al. 2013). For our magnetic polarity this leads to a southward drift, however, in the opposite magnetic polarity these drifts would be northward. In addition, finite Larmor radius effects associated with scattering events produce motion of the guiding centre perpendicular to the magnetic field. The finite Larmor radius effects are more prominent in the  $\lambda = 0.01$  AU panels and they are the cause of the northward displacement. Note that the finite Larmor radius effects do not

have a preferential direction unlike the drifts. They are expected to be more prominent in the more magnetically turbulent simulations as the proton can shift up to 2 Larmor radii per scattering event and there are more scattering events in these simulations.

The longitudinal and latitudinal positions of the protons reiterate that they do not propagate solely along the Parker spiral lines they are initially accelerated on. Therefore, drifts and finite Larmor radius effects are not negligible when determining if protons from the shock are responsible for the observed position of the  $\gamma$ -ray emission region on the solar disc, especially in the high scattering case as a large proportion of the precipitating protons precipitate at later times. Protons with greater energy show stronger deviations from their orig-

inal Parker spiral field lines, even for more early precipitating protons, due to the increase in drifts and finite Larmor radius effects with increasing particle energy. This is clear when comparing panels c) and d) with panels a) and b) in Figure 8.

Note that we have only considered a unipolar Parker spiral magnetic field. Positions on the solar disc are likely to be altered by the more complex coronal magnetic field structure.

## 7. DISCUSSION AND CONCLUSIONS

Magnetic mirroring has been suggested by several authors (e.g., Hudson (2018); Klein et al. (2018)) as a problem for  $>300$  MeV proton back-precipitation and therefore as a difficulty for the CME-shock acceleration scenario for explaining LDGRFs. In this paper we have investigated the problem extensively using 3D test particle simulations.

We derived an analytical expression for the mirror point radius in a Parker spiral magnetic field for scatter-free conditions (Equation 2) showing, as expected, that the mirror point radius increases with the radial height of injection. Therefore, the back precipitation process is more difficult for protons that are injected further from the Sun.

Our results show that back-precipitation is generally highly inefficient, with instantaneous precipitation fractions,  $P$ , for injection at a fixed height, being below 3% in most of our simulations.  $P$  decreases strongly with height of injection,  $r_i$  (Figure 4), e.g. via a power law with an index of -1.78 for a scattering mean free path  $\lambda = 0.1$  AU.

We also found that the presence of scattering facilitates back-precipitation. For example  $P$  increases from 0.138 % to 1.38 % when  $\lambda$  decreases from 1.0 AU to 0.0075 AU, for  $r_i = 20 R_\odot$ . There is, however, a limit to this increase because when the scattering mean free path becomes too small particles are convected with the solar wind and can no longer back-precipitate.

Our simulations show that with increasing radial distance of injection the emission region on the solar surface moves westwards. Particles that precipitate early in time after injection tend to follow Parker spiral magnetic field lines, but with increasing propagation time the protons deviate from their original Parker spiral lines due to drifts and finite Larmor radius effects. This deviation becomes larger with increasing particle energy (Figure 8).

We have applied the above results to 8 specific solar eruptive events which resulted in LDGRFs. LDGRF events are often accompanied by very fast CME-driven shocks: a shock with the average speed of our subset of

events could cover the distance displayed in Figure 4 (5 - 70  $R_\odot$ ) in less than 6.7 hours. The fastest shock would cover this distance in  $\sim 4$  hours and 52 minutes.

By using the radial dependence of instantaneous precipitation and the actual CME-shock speed for the 8 events, assuming constant deceleration and uniform proton shock acceleration with  $r_i$ , we have estimated their total precipitation fractions,  $\bar{P}$ . These range from 0.230% to 1.992%, with the smallest values corresponding to events with the longest durations or fastest shocks. This is because the shocks for these events spend less time close to the solar surface, where the precipitation is efficient, and spend a greater amount of time accelerating particles further from the solar surface where the precipitation fraction is low. The radial position of initial particle injection ( $r_{ini}$ ) has a substantial effect on the total precipitation fraction.

For the CME-driven shock to be the source of the energetic protons causing the  $\gamma$ -ray emission in LDGRFs, observations show that back-precipitation needs to be extended in time (Share et al. 2018) and characterised by large total precipitation values (de Nolfo et al. 2019). However, we have shown that short lived injections (with most of the particle acceleration taking place close to the Sun) are associated with higher precipitation fractions (Figure 7), but when the particle acceleration becomes time-extended the total precipitation fractions become smaller (Figure 7).

In summary the above results present a challenge to the CME-shock acceleration scenario for LDGRFs as follows:

- At times long after the eruptive event at the Sun CME-shocks are very far from the Sun and back-precipitation is extremely difficult. A faster CME-shock only exacerbates this problem.
- The values of total precipitation fraction,  $\bar{P}$  obtained in our study are typically smaller than 10%, while work by de Nolfo et al. (2019) has indicated that in many LDGRF events a much larger value of  $\bar{P}$  is required.
- Time-extended acceleration and large total precipitation fractions cannot be reconciled according to our simulations. A model of an event that makes the duration of the acceleration longer will result in smaller total precipitation fractions.
- The specific shape of the decrease of the precipitation fraction with  $r_i$  would produce a decay in the LDGRF profile that is faster in time than that observed.

For specific LDGRF events our model calculations produce precipitation fractions much smaller than those required to reconcile  $\gamma$ -ray and SEP proton observations via the CME-driven shock scenario (de Nolfo et al. 2019). For two LDGRF events (2011-03-07 and 2012-01-23) they are two orders of magnitude smaller.

All of our simulations only considered 300 MeV protons. However, we do not expect a significant difference in total precipitation fractions for higher energy particles as scattering depends on energy only weakly and the magnetic mirror effect does not depend on particle energy.

As magnetic mirroring provides the largest challenge to the successful precipitation of the  $>300$  MeV protons, it is possible that the Heliospheric Current Sheet (HCS) provides a significant role in the propagation of the protons from large distances back to the solar surface. However, the presence of the HCS would incur further drifts and could lead to the emission region moving substantially but may result in higher total precipitation fractions. There have been observations of a CME-trailing current sheet in the 2017 September 10 LDGRF event, as reported by Kocharov et al. (2020), which may also contribute to a more localised precipitation with a higher total precipitation fraction.

Further work is required to fully understand the contribution of the CME-shock acceleration scenario to the production of  $\gamma$ -rays during LDGRFs. Modelling events in detail, especially the complex events that are more difficult to explain using the shock source scenario, such as the 2012-03-07 event, would provide a clearer picture of its contribution. In order to assess whether drift motion along the current sheet plays a significant role in the back-precipitation process, we should examine the effects of including the HCS in further modelling. It is also important to investigate the role of coronal magnetic configurations below the source surface, as the more complex magnetic structure may help or hinder the back-precipitation process. This is especially important due to the significantly larger proportion of the population that precipitate down to the source surface (Figure 5, left panel).

#### ACKNOWLEDGMENTS

A. Hutchinson, S. Dalla and T. Laitinen acknowledge support from the UK Science and Technology Facilities Council (STFC), through a Doctoral Training grant and grant ST/R000425/1

G.A. de Nolfo and A. Bruno are supported by the NASA Heliophysics Internal Science Funding Model.

#### REFERENCES

- Ackermann, M., Allafort, A., Baldini, L., et al. 2017, *ApJ*, 835, 219, doi: [10.3847/1538-4357/835/2/219](https://doi.org/10.3847/1538-4357/835/2/219)
- Afanasiev, A., Aran, A., Vainio, R., et al. 2018, in *Solar Particle Radiation Storms Forecasting and Analysis*, ed. O. E. Malandraki & N. B. Crosby, Vol. 444, 157–177
- Cliver, E. W., Kahler, S. W., & Vestrand, W. T. 1993, *International Cosmic Ray Conference*, 3, 91
- Dalla, S., de Nolfo, G. A., Bruno, A., et al. 2020, *A&A*, 639, A105, doi: [10.1051/0004-6361/201937338](https://doi.org/10.1051/0004-6361/201937338)
- Dalla, S., Marsh, M., Kelly, J., & Laitinen, T. 2013, *Journal of Geophysical Research: Space Physics*, 118, 5979, doi: [10.1002/jgra.50589](https://doi.org/10.1002/jgra.50589)
- de Nolfo, G. A., Bruno, A., Ryan, J. M., et al. 2019, *ApJ*, 879, 90, doi: [10.3847/1538-4357/ab258f](https://doi.org/10.3847/1538-4357/ab258f)
- Gopalswamy, N., Lara, A., Yashiro, S., Kaiser, M. L., & Howard, R. A. 2001, *Journal of Geophysical Research: Space Physics*, 106, 29207, doi: [10.1029/2001JA000177](https://doi.org/10.1029/2001JA000177)
- Gopalswamy, N., Mäkelä, P., Yashiro, S., et al. 2018, *ApJ*, 868, L19, doi: [10.3847/2041-8213/aaef36](https://doi.org/10.3847/2041-8213/aaef36)
- Gopalswamy, N., Xie, H., Akiyama, S., et al. 2013a, *ApJ*, 765, L30, doi: [10.1088/2041-8205/765/2/L30](https://doi.org/10.1088/2041-8205/765/2/L30)
- Gopalswamy, N., et al. 2013b, *Adv. Space Res.*, 51, 1981, doi: [10.1016/j.asr.2013.01.006](https://doi.org/10.1016/j.asr.2013.01.006)
- Grechnev, V. V., Kiselev, V. I., Kashapova, L. K., et al. 2018, *SoPh*, 293, 133, doi: [10.1007/s11207-018-1352-z](https://doi.org/10.1007/s11207-018-1352-z)
- Hu, J., Li, G., Ao, X., Zank, G. P., & Verkhoglyadova, O. 2017, *Journal of Geophysical Research: Space Physics*, 122, 10,938, doi: <https://doi.org/10.1002/2017JA024077>
- Hudson, H. S. 2018, in *IAU Symposium*, Vol. 335, *Space Weather of the Heliosphere: Processes and Forecasts*, ed. C. Foullon & O. E. Malandraki, 49–53
- Joshi, N., Uddin, W., Srivastava, A., et al. 2013, *Advances in Space Research*, 52, 1, doi: <https://doi.org/10.1016/j.asr.2013.03.009>
- Kahler, S. W., Cliver, E. W., & Kazachenko, M. 2018, *ApJ*, 868, 81, doi: [10.3847/1538-4357/aae9d8](https://doi.org/10.3847/1538-4357/aae9d8)
- Klein, K.-L., Tziotziou, K., Zucca, P., et al. 2018, in *Solar Particle Radiation Storms Forecasting and Analysis*, ed. O. E. Malandraki & N. B. Crosby, Vol. 444, 133–155
- Kocharov, L., Laitinen, T., Vainio, R., et al. 2015, *ApJ*, 806, 80, doi: [10.1088/0004-637X/806/1/80](https://doi.org/10.1088/0004-637X/806/1/80)
- Kocharov, L., Pesce-Rollins, M., Laitinen, T., et al. 2020, *ApJ*, 890, 13, doi: [10.3847/1538-4357/ab684e](https://doi.org/10.3847/1538-4357/ab684e)

- Kong, X., Guo, F., Chen, Y., & Giacalone, J. 2019, *The Astrophysical Journal*, 883, 49, doi: [10.3847/1538-4357/ab3848](https://doi.org/10.3847/1538-4357/ab3848)
- Kouloumvakos, A., Rouillard, A. P., Share, G. H., et al. 2020, *ApJ*, 893, 76, doi: [10.3847/1538-4357/ab8227](https://doi.org/10.3847/1538-4357/ab8227)
- Mandzhavidze, N., & Ramaty, R. 1992, *ApJ*, 396, L111, doi: [10.1086/186529](https://doi.org/10.1086/186529)
- Marsh, M. S., Dalla, S., Dierckxsens, M., Laitinen, T., & Crosby, N. B. 2015, *Space Weather*, 13, 386, doi: [10.1002/2014SW001120](https://doi.org/10.1002/2014SW001120)
- Marsh, M. S., Dalla, S., Kelly, J., & Laitinen, T. 2013, *ApJ*, 774, 4, doi: [10.1088/0004-637x/774/1/4](https://doi.org/10.1088/0004-637x/774/1/4)
- Omodei, N., Pesce-Rollins, M., Longo, F., Allafort, A., & Krucker, S. 2018, *ApJL*, 865, L7, doi: [10.3847/2041-8213/aae077](https://doi.org/10.3847/2041-8213/aae077)
- Owens, M. J., & Forsyth, R. J. 2013, *Living Reviews in Solar Physics*, 10, doi: [10.12942/lrsp-2013-5](https://doi.org/10.12942/lrsp-2013-5)
- Pesce-Rollins, M., Omodei, N., Petrosian, V., et al. 2015, *ApJL*, 805, L15, doi: [10.1088/2041-8205/805/2/L15](https://doi.org/10.1088/2041-8205/805/2/L15)
- Reames, D. V. 2009, *ApJ*, 706, 844, doi: [10.1088/0004-637x/706/1/844](https://doi.org/10.1088/0004-637x/706/1/844)
- Richardson, I. G., von Rosenvinge, T. T., Cane, H. V., et al. 2014, *Solar Physics*, 289, 3059, doi: [10.1007/s11207-014-0524-8](https://doi.org/10.1007/s11207-014-0524-8)
- Ryan, J. M. 2000, *SSRv*, 93, 581, doi: [10.1023/A:1026547513730](https://doi.org/10.1023/A:1026547513730)
- Ryan, J. M., & Lee, M. A. 1991, *ApJ*, 368, 316, doi: [10.1086/169695](https://doi.org/10.1086/169695)
- Share, G. H., Murphy, R. J., White, S. M., et al. 2018, *ApJ*, 869, 182, doi: [10.3847/1538-4357/aaebf7](https://doi.org/10.3847/1538-4357/aaebf7)
- Winter, L. M., Bernstein, V., Omodei, N., & Pesce-Rollins, M. 2018, *ApJ*, 864, 39, doi: [10.3847/1538-4357/aad3c0](https://doi.org/10.3847/1538-4357/aad3c0)
- Zank, G. P., Li, G., Florinski, V., et al. 2006, *Journal of Geophysical Research: Space Physics*, 111, doi: [https://doi.org/10.1029/2005JA011524](https://doi.org/https://doi.org/10.1029/2005JA011524)